INORGANIC CHEMISTRY FRONTIERS

RESEARCH ARTICLE

View Article Online
View Journal

Cite this: DOI: 10.1039/d5qi02340h

Tunable dielectric nanoarchitectonics in carbon nanotubes *via* DNA-directed Pd(II) nanoarrays

Victor K. Abdelkader-Fernández, *†[a] Mikel García-Palomo,†[b] Antonio Pérez-Romero,[a] Francisco G. Ruiz,[b] Andrés Godoy,[b] Manuel Pérez-Mendoza [a] and Miguel A. Galindo *[a]

Received 18th November 2025,
Accepted 14th January 2026

DOI: 10.1039/d5qi02340h

rsc.li/frontiers-inorganic

The precise spatial organization of metal species on carbon nanotube (CNT) surfaces is crucial for tailoring their electronic and dielectric properties, yet remains difficult to achieve in a controlled manner. Here, we report a CNT-based nanohybrid in which one-dimensional Pd(II) arrays, templated by single-stranded DNA (dA_{15}), are covalently anchored onto carboxyl-functionalized multi-walled CNTs. Building on our previous demonstration of continuous helical Pd–DNA architectures, we translate this structural precision to CNT surfaces, yielding uniformly decorated nanotube scaffolds. Comprehensive spectroscopic and microscopic analyses (FTIR, UV–Vis, TEM/HRTEM, EDS) confirm successful assembly and nanoscale organization. Electrical impedance spectroscopy reveals that the resulting CNT–DNA–Pd hybrid exhibits a distinct, tunable dielectric response compared to its individual components. This approach provides a versatile strategy for integrating programmable DNA-based metal architectures with carbon nanomaterials for potential applications in electronics and energy-related devices.

Introduction

Functionalization of carbon nanotubes (CNTs) is essential to unlock their full potential in a wide range of applications, including structural materials, (bio)sensing, electronics, energy storage, environmental remediation, and biomedicine.[1–7] By tailoring their surface chemistry, properties such as chemical reactivity, dispersibility, adsorption, catalytic performance, and electrical conductivity can be significantly enhanced. Over the past two decades, extensive efforts have been devoted to the development of both covalent and non-covalent strategies for decorating CNTs with diverse structural motifs.[8–13] Despite these advances, achieving a controlled and well-defined arrangement of molecules or metals on CNT surfaces is still challenging. In this context, we have been actively exploring new covalent functionalization methodologies for CNTs, employing a variety of functional groups and nanostructures including halogens, oxygen-containing moieties, hyperbranched polyamines, and palladium or platinum nanoparticles.[14–21] In particular, the precise spatial organization of metal species along the nanotube surface and the control of their oxidation states are of great interest, as they directly influence the electrical properties of the resulting nanocomposites.[22,23] Following this foundation, we have built upon previous studies demonstrating the use of DNA oligonucleotides as templates for ordering metal ions and metal complexes at the nanoscale.

The versatility of DNA as a programmable molecular system to generate novel nanoarchitectures, especially in combination with metals, attracts intense interest in nanoelectronics, optics, sensing and other cutting-edge fields.[24–33] In this context, the search for methodologies capable of yielding highly organized metal–DNA assemblies, where the metal ions presence endows DNA molecules with new chemical–physical–structural features (*e.g.*, conductivity, fluorescence, or magnetism), becomes an area of intense research interest, aiming to exploit the extraordinary ability of DNA to rationally interact with metallic matter at the nanoscale and create new molecular systems.[34] We previously demonstrated that Pd(II) complexes can be organized along single-stranded DNA molecules (ssDNA) in a controlled manner, selectively occupying Watson–Crick nucleobases recognition sites.[35,36] In these assemblies, the metal ions form a continuous one-dimensional arrangement dictated by the DNA template, positioning themselves in a precise linear atom-to-atom fashion. Moreover, the ligands coordinated to the Pd(II) centers follow the same chiral trajectory, giving rise to a well-defined Pd–DNA supramolecular helical architecture.

[a]*Departmento de Química Inorgánica, Unidad de Excelencia Química Aplicada a Biomedicina y Medioambiente, Facultad de Ciencias, Universidad de Granada (UGR), Avenida de Fuentenueva, s/n, 18071 Granada, Spain.*
E-mail: victorkarim@ugr.es, magalindo@ugr.es
[b]*Pervasive Electronics Advanced Research Laboratory (PEARL), Departamento de Electrónica y Tecnología de Computadores, Facultad de Ciencias, Universidad de Granada (UGR), Avenida de Fuentenueva, s/n, 18071 Granada, Spain*
†These authors contributed equally to this work.

Guided by these results, we envisioned translating the precise one-dimensional Pd–DNA nanoarrays from solution to the surface of CNTs. In doing so, our goal is not only to uniformly organize the Pd(II) centers helically around the nanotube exterior, but also to introduce a controllable supramolecular interface capable of modulating the dielectric behavior of the CNTs. By using DNA as a programmable template for Pd (II) positioning, we seek to create tunable CNT–DNA–Pd nanoarchitectures in which the electronic environment of the nanotube can be rationally tailored. This strategy enables CNT functionalization through the precise structural control and chiral arrangement offered by DNA-templated Pd(II) arrays, leading to the formation of well-defined, multicomponent nanohybrids. Previous electrochemical impedance spectroscopy (EIS) studies on metal–DNA systems have shown that metal coordination can significantly modify the charge-transfer properties of DNA layers.[27,37,38] However, these effects have been explored almost exclusively in surface-bound films and remain largely unexamined in dispersed hybrid nanostructures. Another study using single-molecule break-junction measurements with SWNTs has shown that metal–DNA systems can enhance charge transport through DNA.[39]

For our work, we selected multi-wall carbon nanotubes functionalized with –COOH groups (**CNT–COOH**), which were covalently coupled to a 15-adenine oligonucleotide functionalized with terminal amino group at the 3′ end (**dA_{15}**). This DNA-functionalized CNT scaffold then serves as the template for the self-assembly of the coordination compound [Pd(Cheld)(CH_3CN)] (Cheld = chelidamic acid) (**1Pd**), as previously reported by our group.[35,36] The synthetic sequence used to prepare the **CNT–dA_{15}–Pd** nanohybrid is illustrated in Fig. 1. To investigate the dielectric of these supramolecular assemblies, we characterized the individual components and their corresponding hybrids using EIS, and the resulting data were analyzed with an equivalent-circuit model.

Results and discussion

Covalent attachment of oligonucleotide dA_{15} to carbon nanotubes (CNT–COOH)

Carboxyl groups on the surface of **CNT–COOH** served as anchoring points for a coupling reaction with the terminal amino group of **dA_{15}**, forming amide bridges between the nanotube surface and the oligonucleotide to yield the **CNT–dA_{15}** compound. The attachment reaction was monitored using UV-vis spectroscopy registered at different times until no variances were observed. The comparison of the UV-vis spectra at the start (t_0) and end (t_f) showed a decrease in the band center at 260 nm, corresponding to the absorption of **dA_{15}**, in agreement with a decrease in concentration due to its incorporation into the carbon nanotubes (Fig. S2). The solid was then centrifuged and subjected to a quick wash to remove unreacted oligonucleotide left free in solution. The solid was then analyzed by means of XPS and the detection of P atoms in the wide spectrum of the **CNT–dA_{15}** hybrid (Fig. S3) unequivocally confirms the presence of **dA_{15}**. Table 1 summarizes the surface composition of the different samples. The P atomic concentration in **CNT–dA_{15}**, in conjunction with the molar mass of **dA_{15}** (4773.26 g mol^{-1}), has allowed for the calculation of a substantial **dA_{15}** content of ≈15 wt%. Furthermore, the increases in O and N in **CNT–dA_{15}** compared to **CNT–COOH**, +3.2 and +4.1 at%, respectively, are consistent with the detected amount of **dA_{15}** and its stoichiometric formula, $C_{153}H_{189}N_{76}O_{76}P_{15}$.

High-resolution XPS spectra further confirms the presence of **dA_{15}** in the **CNT–dA_{15}** hybrid. Fig. 2a compares the normalized C 1s profiles of the three samples. The **CNT–COOH** profile shows an increase in intensity around 288.5 eV, indicating its –COOH functionalization.[40] In the **CNT–dA_{15}** profile, a significant increase is observed from ≈285 eV to ≈289 eV, corresponding to C atoms bonded to O or N,[41] *i.e.*, the carbon backbone of **dA_{15}**. See C 1s deconvolutions for each sample in Fig. S4. Additionally, the N 1s peak deconvolution of **CNT–dA_{15}** (Fig. 2b) reveals two components that can be related to N atoms in the purine skeleton (399.1 eV) and amino groups (400.4 eV) in the adenine base.[42,43] This last component can be also related to the N atom of amide bridge formed between **dA_{15}** and the nanotube surfaces.[44] The [3/2] component at 133.2 eV in P 2p peak deconvolution (Fig. 2c) is attributable to the phosphate groups in **dA_{15}**.[45–47]

High-Resolution TEM and elemental mapping (HRTEM/EDS) further support immobilization of **dA_{15}** on CNT surfaces, as shown in Fig. 2d, where N and P are co-localized along the nanotube contour (additional maps and EDS spectra in Fig. S5

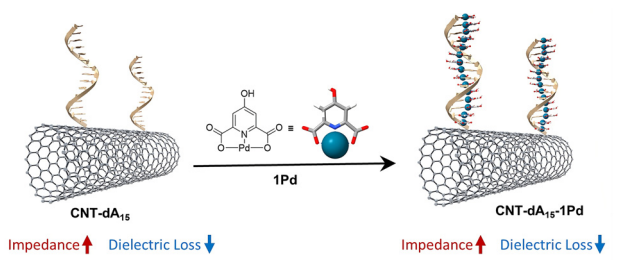

Fig. 1 Schematic representation of the formation of **CNT–dA_{15}–1Pd** hybrids and its electronic properties trends.

Table 1 Surface element composition (XPS) of pristine CNT and modified materials

	XPS concentration (at%)[a]/(wt%)[b]			
Sample	C	O	N	P
CNT	98.9/98.6	1.1/1.4	—	—
CNT–COOH	91.7/89.2	8.3/10.8	—	—
CNT–dA_{15}	83.9/79.6	11.5/14.5	4.1/4.5	0.6/1.5

[a] Surface atomic percentages derived from C 1s, O 1s, N 1s and P 2p region areas in the wide spectra (see XPS wide spectra for all the samples in Fig. S3). [b] Surface mass concentrations calculated from the corresponding atomic values.

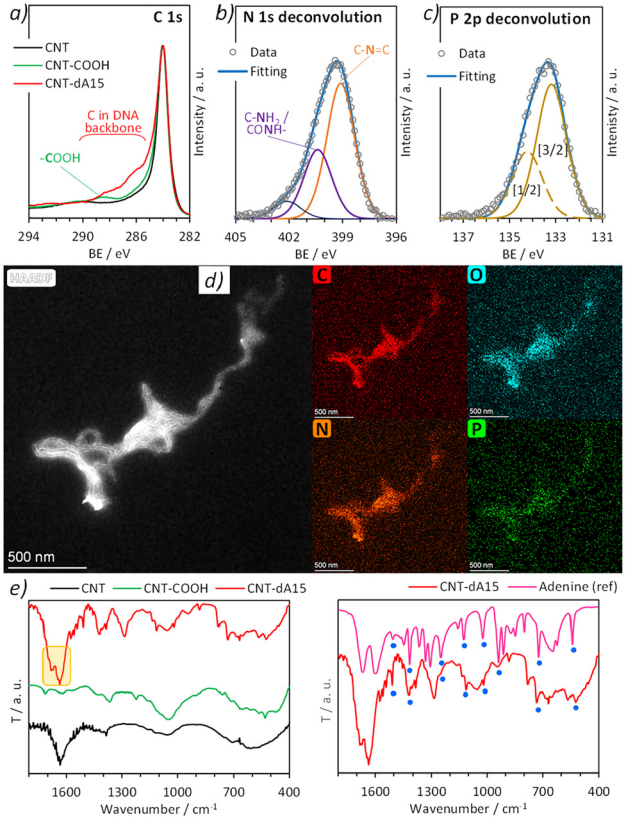

Fig. 2 (a) XPS high-resolution C 1s regions of CNT, **CNT–COOH**, and **CNT–dA$_{15}$**. Deconvolutions of the XPS high-resolution, (b) N 1s and, (c) P 2p core-level peaks for **CNT–dA$_{15}$**, (d) HRTEM micrograph and EDS element distribution maps of C, O, N and P for the **CNT–dA$_{15}$** hybrid, (e) IR spectra of CNT, **CNT–COOH**, and **CNT–dA$_{15}$**, and comparison of **CNT–dA$_{15}$** and adenine reference IR spectra. Blue dots mark peaks common to both spectra.

and S6). FTIR results displayed in Fig. 2e, two prominent bands in the **CNT–dA$_{15}$** spectrum (located at 1640–1680 cm^{-1}) stand out, attributable to the carbonyl stretch vibration within the amide group,[48] consistent with formation of covalent anchoring of **dA$_{15}$** to the nanotubes. Additionally, comparing the spectrum of the hybrid material with the adenine reference spectrum (NIST)[49] in Fig. 2f reveals common IR features, supporting the presence of the oligonucleotide. Additionally, the observation of two weak bands at ≈2850 and ≈2930 cm^{-1} in (Fig. S7) has also been described as indicative of organic macromolecules of a biological nature, such as DNA and proteins.[48]

Preparation of CNT–dA$_{15}$–1Pd hybrid systems

After connecting **dA$_{15}$** onto the nanotube surface, the **1Pd** complexes were subsequently assembled along the DNA strand, adding a new level of structural organization to the hybrid. The self-assembly of **1Pd** with **dA$_{15}$** single strands has been reported previously, and the same procedure was applied in this study to obtain the multicomponent **CNT–dA$_{15}$–1Pd** hybrid.[36] An aqueous dispersion of solubilized **CNT–dA$_{15}$** was titrated with increasing amounts of **1Pd** and the reaction was monitored by means of circular dichroism (CD). Before adding **1Pd** complex, the CD spectrum of **CNT–dA$_{15}$** exhibited a weak and noisy signal, attributed to the intrinsic dispersity of the sample arising from the presence of carbon nanotubes (Fig. 3a). Upon incremental addition of **1Pd**, an increase in ellipticity at 260 nm accompanied by a decrease at 300 nm is observed, and the CD profile progressively evolves into a more defined sinusoidal shape. These spectral changes are consistent with the interaction of **1Pd** with **dA$_{15}$** and the formation of a helical structure stabilized by palladium-mediated base pairs, in agreement with previous reports.[36] A control experiment performed with **CNT–COOH**, in the absence of **dA$_{15}$**, showed that the addition of **1Pd** induces a ellipticity increase at 280 nm (Fig. 3b), likely arising from interactions between aromatic-planar **1Pd** and the nanotube surface. However, these interactions do not produce the characteristic sinusoidal CD profile observed in the presence of **dA$_{15}$**. Therefore, the spectral changes in Fig. 3a can be attributed exclusively to the self-assembly of **1Pd** on the oligonucleotide within **CNT–dA$_{15}$**. Furthermore, UV-vis spectroscopy (Fig. 3c) provides additional evidence of the **1Pd**–adenine base interaction in **CNT–dA$_{15}$–1Pd**, as indicated by the shift of the maximum to shorter wavelengths, ≈275 nm, compared to the free complex, ≈300 nm.

HRTEM/EDS measurements revealed the multicomponent architecture of **CNT–dA$_{15}$–1Pd**, with atoms of P, N, and Pd, indicating that **dA$_{15}$** and **1Pd**, are distributed along the carbon nanotube (Fig. 4 and Fig. S8–S10).

Dielectric properties of CNT–dA$_{15}$–1Pd hybrid systems

The electrical properties of the **CNT–dA$_{15}$–1Pd** hybrids were evaluated by electrical impedance spectroscopy (EIS). Building on the spectroscopic evidence supporting the formation of the **1Pd–dA$_{15}$** assemblies on the CNT, we aimed to assess how their incorporation modulates the electronic properties of the CNTs. In particular, the well-defined one-dimensional Pd arrangement provided by the **1Pd–dA$_{15}$** system offers a con-

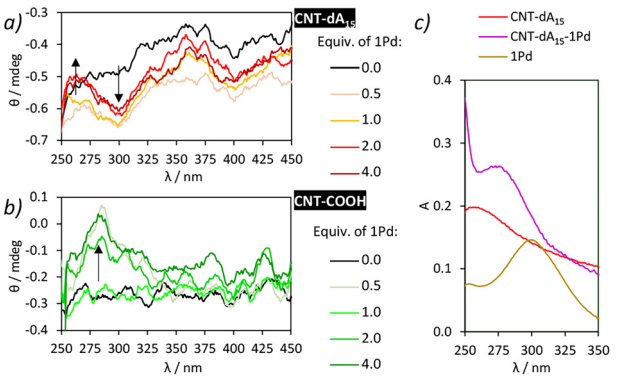

Fig. 3 CD titration spectra for the reaction of **1Pd** with (a) **CNT–dA$_{15}$**, and (b) **CNT–COOH**; the samples were UV-Vis normalized to similar optical density, excluding the 260 nm DNA band (note: 1 equivalent means one **1Pd** per adenine base). (c) Comparison of the UV-vis spectra of **1Pd**, **CNT–dA$_{15}$**, and **CNT–dA$_{15}$–1Pd** sample.

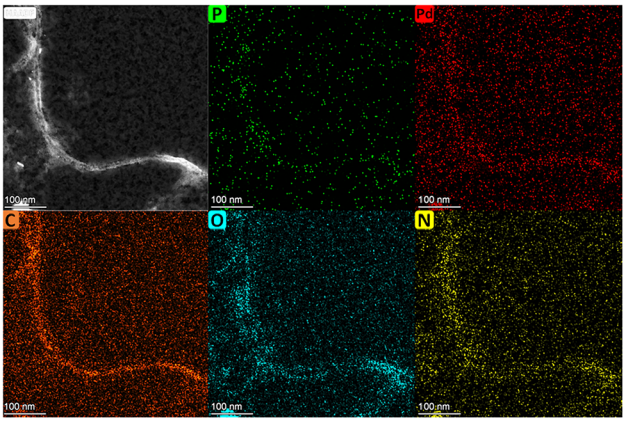

Fig. 4 HRTEM micrograph and EDS element distribution maps of P, Pd, C, O and N for the **CNT–dA$_{15}$–1Pd** hybrid.

trolled means to influence the dielectric response of the resulting **CNT–dA$_{15}$–1Pd** hybrid material. EIS measurements were carried out on aqueous solutions containing diverse samples. One solution contained the **CNT–dA$_{15}$–1Pd** hybrid, while the other two contained the free **1Pd** complex and the **1Pd–dA$_{15}$** system, respectively. All solutions were prepared with the same concentration of the complex to avoid any influence due to concentration differences. Additionally, two control solutions were evaluated, both of which avoid the presence of **1Pd**. One corresponded to the pure solvent (MOPS buffer and DMF), and the other contained **CNT–dA$_{15}$**. Since all samples were prepared in the same aqueous medium and measured under identical temperature and AC excitation conditions, the differences detected in their dielectric parameters can be attributed to the materials present in each sample.

Thus, EIS measurements were performed on five solutions (**CNT–dA$_{15}$–1Pd**, **1Pd**, **1Pd–dA$_{15}$**, **CNT–dA$_{15}$**, and solvent) together with the empty fixture used to determine the reference capacitance (C_0). Fig. 5a shows the Bode plots of the complex impedance, displaying its magnitude and phase *versus* frequency, while Fig. 5b shows the corresponding Nyquist plots ($-\mathrm{Im}(Z_{eq})$ *versus* $\mathrm{Re}(Z_{eq})$). It should be noted that the impedances displayed in Fig. 5 (Bode and Nyquist) were extracted directly from measurements performed with the

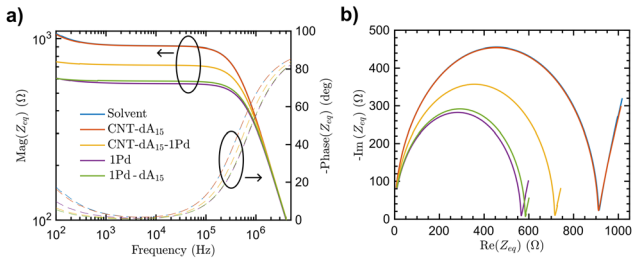

Fig. 5 (a) Real and imaginary part of the measured complex impedances in the frequency range between 100 Hz and 5 MHz. (b) Nyquist diagrams from 100 Hz to 5 MHz. (Note that solvent and **CNT–dA$_{15}$** curves are almost fully overlapping in both plots.)

16452A parallel-plate fixture, without additional post-processing or equivalent circuit fitting.

From Fig. 5a, we observe a null phase around 5 kHz, corresponding to pure resistive behavior and an increasing contribution of the capacitive term for higher frequencies. The semicircle in the Nyquist plot can be described by an equivalent circuit containing a resistor and a capacitor connected in parallel (Fig. S11a), while the straight line for frequencies below 5 kHz is explained by the mass-transport limitation to and from the electrodes, which can be modeled by the Warburg impedance connected in series with the resistance of the parallel circuit (Fig. S11b).[50] In the frequencies of interest, the magnitude of the impedance shows a noticeable dependence on the composition of the solution. Firstly, the **CNT–dA$_{15}$** solution is indistinguishable from the solvent, indicating that both CNTs and **dA$_{15}$**, in the absence of **1Pd** complex, have no influence on the resulting impedance.

For the **1Pd–dA$_{15}$** and **1Pd** solutions, a significant reduction in impedance was observed in both cases, indicating that the self-assembly of **1Pd** into a nanoarrangement along the **dA$_{15}$** chains has no significant effect on the dielectric properties of the samples.

However, the attachment of **1Pd** complexes to the **CNT–dA$_{15}$**, which *a priori* does not affect the impedance (as previously observed for the **CNT–dA$_{15}$** solution), results in an increase in the measured impedance compared to the **1Pd–dA$_{15}$** and **1Pd** solutions, indicating that the organization of the complexes along the ss-DNA template within the **CNT–dA$_{15}$–1Pd** hybrid increase the resistance.

From the perspective of the **CNT–dA$_{15}$** hybrid, which is incapable of altering the impedance of the resulting solution by itself, it is interesting to observe that the incorporation of **1Pd** does lead to a substantial decrease in impedance from ~900 Ω up to ~700 Ω (see Fig. 5b). The impedance changes observed upon metal coordination indicate that **dA$_{15}$–1Pd** interactions can markedly modulate the electrical response of the **CNT–dA$_{15}$–1Pd** hybrid. While our measurements probe the effective (bulk) response of the dispersion, previous impedance studies on surface-bound DNA architecture have likewise shown that the presence and binding mode of metal ions can alter the measured electrical properties in a metal-responsive manner.[38,51] Accordingly, without implying a direct quantitative comparison between these distinct experimental configurations, our results support the general notion that metal coordination to DNA provides an efficient handle to tune the electrical behavior of DNA-based materials.

Employing the parallel plate capacitance (C_p) and resistance (R_p) extracted, together with the reference capacitance (C_0), the complex dielectric constant $\varepsilon_r = \varepsilon_r' - j\varepsilon_r''$ is evaluated by means of the test fixture[52] and eqn (1)–(3). These equations assume that the R_pC_p model accurately captures the behavior of the SUT (as proved in Fig. S12); therefore, the corresponding results and assumptions are valid for frequencies above 5 kHz.

Fig. 6a shows that at low frequencies the real part of relative dielectric constant (ε_r') extracted from the ratio between parallel and reference capacitance, can be grouped in two groups

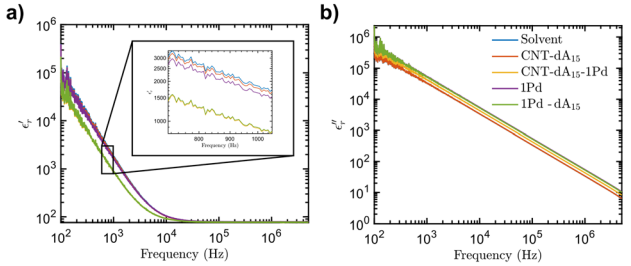

Fig. 6 (a) Relative dielectric constant in the frequency range between 100 Hz and 5 MHz. (b) Dielectric losses in the frequency range 100 Hz–5 MHz.

depending on whether the self-assembly of **1Pd** along $\mathbf{dA_{15}}$ is present in the solution or not. Thereby, the interaction of the **1Pd** complex with the $\mathbf{dA_{15}}$ strands (regardless of whether it is **CNT–dA$_{15}$–1Pd** or **1Pd–dA$_{15}$**, that is, regardless of the immobilization of $\mathbf{dA_{15}}$ chains on the nanotubes) can be identified as the main responsible for the decrease in parallel capacitance, and therefore, for the lower relative dielectric constants. Later, from ~20 kHz frequency onwards, all samples converge to the value established by the solvent.

As for the dielectric losses (ε_r'') depicted in Fig. 6b, the trend is related to the complex impedance behavior (see Fig. 5 and associated comments). The solvent together with **CNT–dA$_{15}$** present lower dielectric losses, appreciating a clear increment in the conductivity with **CNT–dA$_{15}$–1Pd** and even higher with the **1Pd** and **1Pd–dA$_{15}$** solutions, a behavior which is mirrored in the solution's impedance. The observed increase in ε_r'' for **CNT–dA$_{15}$–1Pd** compared to **CNT–dA$_{15}$** can be attributed to energy dissipation resulting from the movement of charges in the alternating electric field.[53] Therefore, since the dielectric losses shown by **CNT–dA$_{15}$** are indistinguishable from those of the solvent, this increment serves as an indication of the charge transfer process within the multicomponent hybrid.

Conclusions

In this study, we have demonstrated that by exploiting the specific self-assembly properties of the **1Pd–dA$_{15}$** system, we achieved the formation of continuous one-dimensional Pd(II) arrays directly on DNA strands immobilized on the CNT surface. Circular dichroism spectroscopy confirmed that the **Pd–DNA** architecture formed on the nanotubes reproduces the same ordered helical arrangement previously observed in solution, indicating that the structural integrity of the Pd nanoarrays is preserved upon integration into the CNT-based hybrid. HRTEM/EDS measurements further confirmed the multicomponent architecture of the **CNT–dA$_{15}$–1Pd** hybrids, revealing the presence of P, N, and Pd atoms distributed along the nanotubes, consistent with the localization of both $\mathbf{dA_{15}}$ and the **1Pd** complexes on the CNT framework. Importantly, electrical impedance spectroscopy revealed that the assembly of the Pd (II) complexes on the DNA-functionalized CNTs modulates the dielectric response of the hybrid material. The incorporation of the Pd nanoarrays leads to a measurable decrease in impedance and an increase in dielectric loss, consistent with Pd-to-CNT charge transfer mediated by the DNA scaffold.

Overall, this work shows that DNA–Pd architectures can be reliably formed on CNTs and that their nanoscale organization has a direct impact on the electronic behavior of the resulting hybrid. These findings establish a proof of concept for the design of CNT-based materials whose electrical properties can be tuned through the programmed self-assembly of metal complexes along DNA templates.

Experimental

The materials and reagents used in this study include commercial NC3100™ thin multiwalled carbon nanotubes (CNTs) from Nanocyl SA (Belgium), characterized by a high purity of 95+% carbon. The single-stranded DNA oligonucleotide ($\mathbf{dA_{15}}$) from Sigma-Aldrich (MO, USA) consists of fifteen 2′-deoxyadenosine bases with a terminal amino group (–NH_2) at the 3′ position ($C_{153}H_{189}N_{76}O_{76}P_{15}$, molecular weight = 4773.26). The formula of the palladium complex (**1Pd**) is [Pd(Cheld)(CH_3CN)], where Cheld represents chelidamic acid ($C_7H_5NO_5$). The synthesis of the **1Pd** complex, the formation of the **1Pd–dA$_{15}$** hybrids and the procedures used in this study have been reported elsewhere.[36] We also used 1-ethyl-3-(3-dimethylaminopropyl)carbodiimide hydrochloride (EDC, $C_8H_{17}N_3$·HCl) and *N*-hydroxysuccinimide (NHS, $C_4H_5NO_3$), both sourced from Sigma-Aldrich (MO, USA) and used as commercial grade and for synthesis, respectively. *N*,*N*-Dimethylformamide (DMF, C_3H_7NO), obtained from Sigma-Aldrich (MO, USA), met ACS reagent standards with a purity of ≥99.8%. Additionally, 3-(*N*-morpholino) propanesulfonic acid (MOPS, $C_7H_{15}NO_4S$) was acquired from Sigma-Aldrich (MO, USA) in BioUltra grade for molecular biology applications. Potassium permanganate ($KMnO_4$), also from Sigma-Aldrich (MO, USA), was employed as ACS reagent with purity of ≥99.0%. Milli-Q® water, with a resistance of 18.2 mΩ cm^{-1} (Type I, ultrapure), was used throughout the experiments.

Grafting dA$_{15}$ onto carbon nanotubes

The CNTs were oxidized with $KMnO_4$ to functionalize them with carboxyl groups (–COOH),[54] resulting in the **CNT–COOH** sample. See Experimental Details Section in SI. Then, the covalent anchoring reaction of the $\mathbf{dA_{15}}$ oligonucleotide to **CNT–COOH** was mediated by the prior activation of carboxyl groups with EDC and NHS.[55,56] This coupling reaction ultimately forms amide groups (–CONH–) bridging the nanotube and $\mathbf{dA_{15}}$. The resulting hybrid was labeled as **CNT–dA$_{15}$**. In detail, in the first step, **CNT–COOH** (55 μg) was dispersed in 25 mM $MOPS_{(aq)}$ buffer with pH = 6.5 (189 μL) *via* sonication. Then, coupling agents EDC (0.4 M, 11.70 mg) and NHS (0.027 M, 0.58 mg) were added (NHS : EDC molar ratio of 1 : 15) allowing to stand for 15 minutes. In the second step, 311 μL of 100 μM $\mathbf{dA_{15}}$ solution (in 25 mM $MOPS_{(aq)}$ buffer) were added

to the previously activated **CNT–COOH** dispersion and, subsequently, kept undisturbed at 4 °C, overnight. The resulting suspension was centrifuged (14 000 rpm, 10 min), and the solid washed repeatedly with MOPS buffer until the supernatant did not reveal the presence of $\mathbf{dA_{15}}$ (by measuring UV absorption at 260 nm, Fig. S2). The $\mathbf{CNT–dA_{15}}$ system was characterized using XPS, HRTEM/EDS and FTIR spectroscopy. It is worth mentioning that the sample contained $\mathbf{CNT–dA_{15}}$ of different nanotubes sizes, as commonly observed for commercially available carbon nanotubes.

Self-assembly of complex 1Pd with CNT–dA$_{15}$

The soluble fraction of $\mathbf{CNT–dA_{15}}$ was isolated in MOPS buffer from the insoluble part. To solubilize it, the $\mathbf{CNT–dA_{15}}$ hybrid solid was immersed in 1 mL of 1 mM $MOPS_{(aq)}$ buffer (pH = 6.8), sonicated for 30 seconds, and stirred for 2 hours at 50 °C. After separation *via* centrifugation (14 000 rpm, 10 min), the supernatant was analyzed through UV-vis spectroscopy to confirm the presence of solubilized $\mathbf{CNT–dA_{15}}$ and estimate the concentration of the oligonucleotide (Fig. S1). This allowed calculating the number of adenines bases available to coordinate with **1Pd**. Considering the amount required to achieve a stoichiometric **1Pd** : adenine ratio of 1 : 1 as one equivalent, a titration was performed by adding controlled amounts of complex **1Pd** (incremental equivalents) to monitor the self-assembly. This titration was tracked by circular dichroism (CD). The resulting multicomponent material is named $\mathbf{CNT–dA_{15}–1Pd}$. In detail, the solubilized $\mathbf{CNT–dA_{15}}$ sample (stock solution) for the CD spectroscopy titration series presented an oligonucleotide concentration of *ca.* 0.8 μM (see Fig. S1). An initial $\mathbf{CNT–dA_{15}}$ solution was elaborated by mixing 350 μL of the stock solution with 350 μL of ultrapure water. To this initial solution, the aliquots from a stock solution of **1Pd** (500 μM, DMF) were added, along with comparable aliquots from the $\mathbf{CNT–dA_{15}}$ stock solution to keep the concentration constant. Once the titration experiments have finalized, when 2 equivalents of the complex **1Pd** were present in the solution, the resulting solution contained 6% of DMF. An equivalent control experiment was performed using a **CNT–COOH** dispersion whose concentration was adjusted by UV-Vis normalization to match the optical density of $\mathbf{CNT–dA_{15}}$, excluding the 260 nm band associated with DNA absorption.

Physicochemical characterization

Different techniques were implemented to achieve a comprehensive physicochemical characterization. Ultraviolet-visible (UV-vis) spectroscopy was conducted using a Varian Cary-Eclipse spectrophotometer, equipped with a xenon lamp (peak power 75 kW), a CZERNY-Turner monochromator, and an R-298 red-sensitive photomultiplier tube. Fourier transform infrared (FTIR) spectroscopy was performed on a Jasco FT/IR-460 Plus spectrophotometer, covering the range of 400–4000 cm^{-1} with a resolution of 4 cm^{-1} and 64 scans. X-ray photoelectron spectroscopy (XPS) measurements were carried out using a Kratos Axis Ultra-DLD spectrometer with an Al/Mg twin anode. Monochromatic Kα radiation was used in constant-analyzer-energy mode with pass energies of 160 and 20 eV for survey and high-resolution spectra, respectively. High-resolution transmission electron microscopy (HRTEM) coupled with energy dispersive X-ray spectroscopy (EDS) was performed using an FEI TITAN G2 microscope with selectable acceleration voltage from 50 to 300 kV, a maximum magnification of 1.25 MX, a resolution of 0.8 Å, and an XFEG-type field emission gun with a Schottky-type filament. The EDS analysis was conducted using the FEI microanalysis system equipped with four detectors and an image drift correction system. Finally, circular dichroism (CD) spectroscopy was carried out with a Jasco J-815 spectropolarimeter, which includes a Peltier temperature controller.

Measurements of dielectric properties

EIS measurement setup details & calibration. In the pursuit of characterizing the electrical properties of various solutions making use of the Electrochemical Impedance Spectroscopy (EIS) technique, the Keysight E4990A impedance analyzer has been employed, operating within a frequency range spanning from 20 Hz to 120 MHz.[57] The analyzer (Fig. S13) was supplemented with the Keysight 16048G port extension[58] in conjunction with the Keysight 16452A Liquid Test Fixture,[52] designed for experimental measurements within the frequency range of 20 Hz–30 MHz. The adoption of a 4-terminal pair (4TP) measurement technique serves to minimize measurement errors by mitigating the influence of parasitics such as contact resistances, residual impedances, and short and open offsets. The calibration process entails a sequential methodology beginning with the calibration of the port extension (16048G) employing a 100 Ω load (Keysight E4990-61051). Then, the 16452A fixture was calibrated incorporating a short compensation procedure. Stringent criteria are applied to ensure calibration accuracy, requiring that the residual series inductance remains below 20 nH, and the series resistance is maintained below 0.5 Ω.[52]

Dielectric properties extraction. The extraction of the dielectric properties of the solution encompasses two distinct measurements: first, a reference measurement conducted with air-filled fixture, serving as the dielectric medium between two parallel plates, enables the determination of the reference capacitance (C_0) across the desired frequency range. Second, the fixture is filled with the solution and the measurement is carried out in the same frequency range. The auxiliary reference measurement is instrumental in rectifying or mitigating potential measurement errors arising from minor fluctuations in plate separation distance and electrode effective area. The parallel plate spacing was 3 mm, with a required liquid volume of 6.8 ml. The air reference yielded C_0 = 5.3 pF at 1 MHz, close to the target value of 5.5 ± 10% pF at the same frequency.

By employing the measured parallel plate capacitance (C_m) and resistance (R_m), in conjunction with C_0, the complex dielectric constant ($\varepsilon_{rm} = \varepsilon'_{rm} - j\varepsilon''_{rm}$) is evaluated as:

$$\varepsilon_{rm} = \varepsilon'_{rm} - j\varepsilon''_{rm} = \frac{C_m}{C_0} - j\frac{1}{\omega C_0 R_m} \quad (1)$$

where ω is the angular frequency. To account for fringing effects of the 16452A fixture, a correction factor α was applied:

$$\alpha = \frac{100|\varepsilon_{rm}|}{97.0442|\varepsilon_{rm}| + 2.9558}, \varepsilon_r = \alpha\varepsilon_{rm} \quad (2)$$

where ε_r is the corrected complex dielectric constant. Furthermore, the conductivity (σ) is determined by the dielectric losses (ε_r''):

$$\sigma = \varepsilon_0\varepsilon_r''\omega = \varepsilon_0\alpha\varepsilon_{rm}''\omega = \frac{\varepsilon_0\alpha}{C_0R_m} \quad (3)$$

with ε_0 the vacuum permittivity.

The accurate extraction of the dielectric properties requires that the equivalent model of the measured impedance conforms to a parallel R|C configuration. The analysis of the Nyquist plot indicates that for frequencies above 5 kHz, this equivalent model of the Samples Under Test (SUT) can be assumed. Nevertheless, in instances involving samples with elevated conductivity, such as cell suspensions, the polarization impedance at the electrodes, operating in series with the SUT impedance, cannot be disregarded. Various methodologies exist to approximate this behavior, typically involving attempts to offset its influence.[44,45] In the context of the current investigation, attention is directed towards a frequency range wherein this effect can be deemed negligible.

Although the operational frequency range of the experimental setup (E4990A impedance analyzer, 16048G extension port, and 16452A fixture) covers the 20 Hz–30 MHz range, we limit the usable window to 1 kHz–5 MHz to minimize noise and polarization artifacts. At sufficiently low frequencies (<1 kHz), the polarization impedance Z_{pol} (modelling the electrode behavior) becomes dominant, as evidenced in Fig. S14a and based on the Nyquist plot, for frequencies below 5 kHz, the SUT impedance no longer fits a parallel RC model. Polarization impedance typically exhibits a reactive nature (as the compounds under study), converging towards the behavior of the solution as the excitation frequency increases. Such behavior does not manifest in the conductivity of the composites, as depicted in Fig. S14b, given that conductivity is directly associated with the real part of the measured impedance, related to R_m.

Conflicts of interest

There are no conflicts to declare.

Author contributions

V. K. A.-F. and A. P.-R. prepared and characterized the molecular systems and contributed to data analysis and discussion. M. G.-P., F. G. R., and A. G. performed the electronic studies, and analyzed and discussed the corresponding data. M. A. G. and V. K. A.-F. conceived the research and wrote the original draft, leading manuscript preparation. M. A. G. and M. P.-M. supervised the project, analyzed the data, and secured funding. All authors reviewed and approved the final version of the manuscript.

Data availability

All data supporting the findings of this study, including experimental results and characterization data, are provided in the supplementary information (SI). Supplementary information: experimental details: oxidation of CNT *via* $KMnO_4$ treatment. Figures: S1, UV-vis spectrum of the solubilized **CNT–dA$_{15}$** dispersion; S2, UV-vis spectra of CNT–COOH and dA_{15} reaction medium at initial and final times, and the supernatants in wash repetitions; S3, XPS wide spectra of the **CNT**, **CNT–COOH** and **CNT–dA$_{15}$** samples; S4, XPS high-resolution C 1s deconvolutions of the CNT, **CNT–COOH** and **CNT–dA$_{15}$** samples; S5–S6, HRTEM images, EDS spectra and element distribution maps of the **CNT–dA$_{15}$** hybrid; S7, FTIR spectrum of the **CNT–dA$_{15}$** hybrid; S8–S10, HRTEM images, EDS spectra and element distribution maps of the multicomponent **CNT–dA$_{15}$–1Pd** hybrid; S11, (a) parallel capacitance–resistance circuit corresponding to the equivalent electrical model of the SUT, (b) parallel capacitance–resistance circuit including Warburg impedance ($Z\omega$); S12, Fitted parameters for the R_pC_p model; S13, Illustration of the EIS measurement setup; S14, (a) relative dielectric constant ($\varepsilon'r$) and (b) conductivity in the frequency range 1 kHz–5 MHz. See DOI: **https://doi.org/10.1039/d5qi02340h**.

Acknowledgements

Financial support was received from Grant PID2020-120186RB-I00 and PID2023-152026NB-I00 funded by MCIN/AEI/10.13039/501100011033, Grant P20_00702 funded by Consejería de Universidad, Investigación e Innovación and "FEDER – a way of making Europe", Junta de Andalucia. V. K. A.-F thanks the ElectroPlas project (EMERGIA program, EMEC_2023_00163, Plan Andaluz, D. 54/1989, Consejería de Universidad, Investigación e Innovación, Junta de Andalucía) for its financial support. M. G.-P. acknowledges the grant PREP2023-001936 funded by MICIU/AEI/10.13039/501100011033 and FSE+.

References

1 S. Peñas-Núñez, D. Mecerreyes and M. Criado-Gonzalez, Recent Advances and Developments in Injectable Conductive Polymer Gels for Bioelectronics, *ACS Appl. Bio Mater.*, 2024, **7**, 7944–7964, DOI: **10.1021/acsabm.3c01224**.

2 A. Ali, S. Koloor, A. Alshehri and A. Arockiarajan, Carbon nanotube characteristics and enhancement effects on the mechanical features of polymer-based materials and structures-A review, *J. Mater. Res. Technol.*, 2023, **24**, 6495–6521, DOI: **10.1016/j.jmrt.2023.04.072**.

3 J. Zhou, L. Ren, H. Li, X. Cheng, Z. Pan, Z. Zhang, L. Ding and L. Peng, Carbon Nanotube Radiofrequency Transistors With fT/fMAX of 376/318 GHz, *IEEE Electron Device Lett.*, 2023, **44**, 329–332, DOI: **10.1109/LED.2022.3227133**.

4 N. Nurazzi, M. Asyraf, A. Khalina, N. Abdullah, F. Sabaruddin, S. Kamarudin, S. Ahmad, A. Mahat, C. Lee, H. Aisyah, *et al.*, Fabrication, Functionalization, and Application of Carbon Nanotube-Reinforced Polymer Composite: An Overview, *Polymers*, 2021, **13**, 1047, DOI: **10.3390/polym13071047**.

5 F. Khan, N. Mubarak, Y. Tan, M. Khalid, R. Karri, R. Walvekar, E. Abdullah, S. Nizamuddin and S. Mazari, A comprehensive review on magnetic carbon nanotubes and carbon nanotube-based buckypaper for removal of heavy metals and dyes, *J. Hazard. Mater.*, 2021, **413**, 125375, DOI: **10.1016/j.jhazmat.2021.125375**.

6 F. Mustafa and S. Andreescu, Nanotechnology-based approaches for food sensing and packaging applications, *RSC Adv.*, 2020, **10**, 19309–19336, DOI: **10.1039/d0ra01084g**.

7 S. Zhu, J. Ni and Y. Li, Carbon nanotube-based electrodes for flexible supercapacitors, *Nano Res.*, 2020, **13**, 1825–1841, DOI: **10.1007/s12274-020-2729-5**.

8 H. Hosseini and M. Ghaffarzadeh, Surface functionalization of carbon nanotubes via plasma discharge: A review, *Inorg. Chem. Commun.*, 2022, **138**, 109276, DOI: **10.1016/j.inoche.2022.109276**.

9 L. Lavagna, R. Nisticò, S. Musso and M. Pavese, Functionalization as a way to enhance dispersion of carbon nanotubes in matrices: a review, *Mater. Today Chem.*, 2021, **20**, 100477, DOI: **10.1016/j.mtchem.2021.100477**.

10 P. Bilalis, D. Katsigiannopoulos, A. Avgeropoulos and G. Sakellariou, Non-covalent functionalization of carbon nanotubes with polymers, *RSC Adv.*, 2014, **4**, 2911–2934, DOI: **10.1039/c3ra44906h**.

11 A. Di Crescenzo, V. Ettorre and A. Fontana, Non-covalent and reversible functionalization of carbon nanotubes, *Beilstein J. Nanotechnol.*, 2014, **5**, 1675–1690, DOI: **10.3762/bjnano.5.178**.

12 P. Ma, N. Siddiqui, G. Marom and J. Kim, Dispersion and functionalization of carbon nanotubes for polymer-based nanocomposites: A review, *Composites, Part A*, 2010, **41**, 1345–1367, DOI: **10.1016/j.compositesa.2010.07.003**.

13 L. Meng, C. Fu and Q. Lu, Advanced technology for functionalization of carbon nanotubes, *Prog. Nat. Sci.*, 2009, **19**, 801–810, DOI: **10.1016/j.pnsc.2008.08.011**.

14 F. Morales-Lara, V. K. Abdelkader-Fernandez, M. Melguizo, A. Turco, E. Mazzotta, M. Domingo-Garcia, F. J. Lopez-Garzon and M. Pérez-Mendoza, Ultra-small metal nanoparticles supported on carbon nanotubes through surface chelation and hydrogen plasma reduction for methanol electro-oxidation, *J. Mater. Chem. A*, 2019, **7**, 24502–24514, DOI: **10.1039/c9ta08424j**.

15 V. K. Abdelkader-Fernandez, F. Morales-Lara, M. de la Torre, M. Melguizo, F. J. Lopez-Garzon, M. Domingo-Garcia and M. Pérez-Mendoza, HBPEI-grafted carbon nanotubes for the effective retention of Pd2+ and Pt2+ through complexation, *Inorg. Chem. Front.*, 2018, **5**, 1978–1984, DOI: **10.1039/c8qi00320c**.

16 V. K. A. Fernandez, M. Melguizo, C. G. Gallarin, M. de la Torre, M. D. G. Valero, A. M. Alonso, M. D. Garcia, F. J. L. Garzon and M. P. Mendoza, Copper-catalyzed direct amination of the superficial graphenic domains of multi-walled carbon nanotubes, *Catal. Sci. Technol.*, 2017, **7**, 3361–3374, DOI: **10.1039/c7cy00601b**.

17 V. K. Abdelkader, M. Domingo-Garcia, M. Melguizo, R. Lopez-Garzon, F. J. Lopez-Garzon and M. Pérez-Mendoza, Covalent bromination of multi-walled carbon nanotubes by iodine bromide and cold plasma treatments, *Carbon*, 2015, **93**, 276–285, DOI: **10.1016/j.carbon.2015.05.070**.

18 V. K. Abdelkader-Fernandez, F. Morales-Lara, M. Melguizo, C. Garcia-Gallarin, R. Lopez-Garzon, M. L. Godino-Salido, F. J. Lopez-Garzon, M. Domingo-Garcia and M. Pérez-Mendoza, Degree of functionalization and stability of fluorine groups fixed to carbon nanotubes and graphite nanoplates by CF4 microwave plasma, *Appl. Surf. Sci.*, 2015, **357**, 1410–1418, DOI: **10.1016/j.apsusc.2015.09.262**.

19 V. K. Abdelkader, M. Domingo-Garcia, M. D. Gutierrez-Valero, R. Lopez-Garzn, M. Melguizo, C. Garcia-Gallarin, F. J. Lopez-Garzon and M. Pérez-Mendoza, Sidewall Chlorination of Carbon Nanotubes by Iodine Trichloride, *J. Phys. Chem. C*, 2014, **118**, 2641–2649, DOI: **10.1021/jp411935g**.

20 V. K. Abdelkader-Fernández, F. Morales-Lara, M. Melguizo, C. García-Gallarín, R. López-Garzón, M. L. Godino-Salido, F. J. López-Garzón, M. Domingo-García and M. Pérez-Mendoza, Fluorination of graphite nanoplates and multi-wall carbon nanotubes by CF4 cold plasma, *Appl. Surf. Sci.*, 2015, **357**, 1410–1418, DOI: **10.1016/j.apsusc.2015.09.262**.

21 V. K. Abdelkader, S. Scelfo, C. Garcia-Gallarin, M. L. Godino-Salido, M. Domingo-Garcia, F. J. Lopez-Garzon and M. Pérez-Mendoza, Carbon Tetrachloride Cold Plasma for Extensive Chlorination of Carbon Nanotubes, *J. Phys. Chem. C*, 2013, **117**, 16677–16685, DOI: **10.1021/jp404390h**.

22 W. Xia, Interactions between metal species and nitrogen-functionalized carbon nanotubes, *Catal. Sci. Technol.*, 2016, **6**, 630–644, DOI: **10.1039/c5cy01694k**.

23 F. Banhart, Interactions between metals and carbon nanotubes: at the interface between old and new materials, *Nanoscale*, 2009, **1**, 201–213, DOI: **10.1039/b9nr00127a**.

24 G. Q. Yang, W. B. Cai, Z. W. Zhang and Y. J. Wang, Progress in Programmable DNA-Aided Self-Assembly of the Master Frame of a Drug Delivery System, *ACS Appl. Bio Mater.*, 2023, **6**, 5125–5144, DOI: **10.1021/acsabm.3c00636**.

25 B. Kou, Z. C. Wang, S. Mousavi, P. F. Wang and Y. G. Ke, Dynamic Gold Nanostructures Based on DNA Self Assembly, *Small*, 2023, **20**, 2308862, DOI: **10.1002/smll.202308862**.

26 N. Bangruwa, M. Srivastava and D. Mishra, Radiation-Induced Effect on Spin-Selective Electron Transfer through

Self-Assembled Monolayers of ds-DNA, *Magnetochemistry*, 2021, **7**, 98, DOI: **10.3390/magnetochemistry7070098**.

27 M. Hossain, S. Ahmad and H. Kraatz, Consecutive Silver(I) Ion Incorporation into Oligonucleotides containing Cytosine-Cytosine Mispairs, *ChemPlusChem*, 2021, **86**, 224–231, DOI: **10.1002/cplu.202000607**.

28 A. Gonzàlez-Rosell, C. Cerretani, P. Mastracco, T. Vosch and S. Copp, Structure and luminescence of DNA-templated silver clusters, *Nanoscale Adv.*, 2021, **3**, 5, DOI: **10.1039/d0na01005g**.

29 X. P. Dai, Q. Li, A. Aldalbahi, L. H. Wang, C. H. Fan and X. G. Liu, DNA-Based Fabrication for Nanoelectronics, *Nano Lett.*, 2020, **20**, 5604–5615, DOI: **10.1021/acs.nanolett.0c02511**.

30 S. K. Vittala and D. Han, DNA-Guided Assemblies toward Nanoelectronic Applications, *ACS Appl. Bio Mater.*, 2020, **3**, 2702–2722, DOI: **10.1021/acsabm.9b01178**.

31 S. Bagheri, Theoretical study of hydrogen bonds and electronic properties in hexagonal arrangements composed of self-assembled DNA analogues, *Struct. Chem.*, 2020, **31**, 2075–2085, DOI: **10.1007/s11224-020-01545-5**.

32 N. C. Seeman and H. F. Sleiman, DNA nanotechnology, *Nat. Rev. Mater.*, 2018, **3**, 1, DOI: **10.1038/natrevmats.2017.68**.

33 B. Jash and J. Müller, Metal-Mediated Base Pairs: From Characterization to Application, *Chem. – Eur. J.*, 2017, **23**, 17166, DOI: **10.1002/chem.201703518**.

34 Z. Chen, C. Liu, F. Cao, J. Ren and X. Qu, DNA metallization: principles, methods, structures, and applications, *Chem. Soc. Rev.*, 2018, **47**, 4017–4072, DOI: **10.1039/c8cs00011e**.

35 A. Perez-Romero, M. Cano-Muñoz, C. López-Chamorro, F. Conejero-Lara, O. Palacios, J. Dobado and M. Galindo, Selective Formation of Pd-DNA Hybrids Using Tailored Palladium-Mediated Base Pairs: Towards Heteroleptic Pd-DNA Systems, *Angew. Chem., Int. Ed.*, 2024, **63**, 11, DOI: **10.1002/anie.202400261**.

36 A. Pérez-Romero, A. Domínguez-Martín, S. Galli, N. Santamaría-Díaz, O. Palacios, J. Dobado, A. Nyman and M. Galindo, Single-Stranded DNA as Supramolecular Template for One-Dimensional Palladium(II) Arrays, *Angew. Chem., Int. Ed.*, 2021, **60**, 10089–10094, DOI: **10.1002/anie.202015554**.

37 N. Flothkötter, N. Lefringhausen, D. Escher, J. Müller and H. Kraatz, Electrochemical Characterization of Site-Specifically Metal-Modified DNA Films on Gold Electrode Surfaces, *ChemPlusChem*, 2025, **90**, e202500494, DOI: **10.1002/cplu.202500494**.

38 J. C. Léon, Z. She, A. Kamal, M. H. Shamsi, J. Müller and H. B. Kraatz, DNA Films Containing the Artificial Nucleobase Imidazole Mediate Charge Transfer in a Silver (I)-Responsive Way, *Angew. Chem., Int. Ed.*, 2017, **56**, 6098–6102, DOI: **10.1002/anie.201700248**.

39 S. Liu, G. H. Clever, Y. Takezawa, M. Kaneko, K. Tanaka, X. Guo and M. Shionoya, Direct Conductance Measurement of Individual Metallo-DNA Duplexes within Single-Molecule Break Junctions, *Angew. Chem., Int. Ed.*, 2011, **50**, 8886–8890, DOI: **10.1002/anie.201102980**.

40 N. Lachman, X. Sui, T. Bendikov, H. Cohen and H. D. Wagner, Electronic and mechanical degradation of oxidized CNTs, *Carbon*, 2012, **50**, 1734–1739, DOI: **10.1016/j.carbon.2011.12.009**.

41 X. N. Chen, X. H. Wang and D. Fang, A review on C1s XPS-spectra for some kinds of carbon materials, *Fullerenes, Nanotubes Carbon Nanostruct.*, 2020, **28**, 1048–1058, DOI: **10.1080/1536383x.2020.1794851**.

42 Y. Z. Xu, C. L. Chen, M. Zhou, G. Y. Fu, Y. Y. Zhao and Y. H. Chen, Improved oxygen reduction activity of carbon nanotubes and graphene through adenine functionalization, *RSC Adv.*, 2017, **7**, 26722–26728, DOI: **10.1039/c7ra02865b**.

43 M. Pagliai, S. Caporali, M. Muniz-Miranda, G. Pratesi and V. Schettino, SERS, XPS, and DFT Study of Adenine Adsorption on Silver and Gold Surfaces, *J. Phys. Chem. Lett.*, 2012, **3**, 242–245, DOI: **10.1021/jz201526v**.

44 NIST X-ray Photoelectron Spectroscopy (XPS) Database, **https://srdata.nist.gov/xps/**.

45 T. P. Moffat, R. M. Latanision and R. R. Ruf, An X-ray photoelectron-spectroscopy study of chromium-metalloid alloys, *Electrochim. Acta*, 1995, **40**, 1723–1734, DOI: **10.1016/0013-4686(95)00015-7**.

46 J. M. Pembamabiala, M. Lenzi, J. Lenzi and A. Lebugle, XPS study of mixed cerium terbium orthophosphate catalysts, *Surf. Interface Anal.*, 1990, **15**, 663–667, DOI: **10.1002/sia.740151105**.

47 W. E. Morgan, W. J. Stec and J. R. Vanwazer, Inner-orbital photoelectron spectroscopy of alkali-metal halides, perchlorates, phosphates, and pyrophosphates, *J. Am. Chem. Soc.*, 1973, **95**, 751–755, DOI: **10.1021/ja00784a018**.

48 K. Awasthi, D. P. Singh, S. Singh, D. Dash and O. N. Srivastava, Attachment of biomolecules (protein and DNA) to amino-functionalized carbon nanotubes, *New Carbon Mater.*, 2009, **24**, 301–306, DOI: **10.1016/s1872-5805(08)60053-0**.

49 NIST Chemistry WebBook, SRD 69, **https://webbook.nist.gov/cgi/cbook.cgi?ID=C73245&Type=IR-SPEC&Index=2#IR-SPEC**.

50 A. C. Lazanas and M. I. Prodromidis, Electrochemical Impedance Spectroscopy-A Tutorial, *ACS Meas. Sci. Au*, 2023, **3**, 162–193, DOI: **10.1021/acsmeasuresciau.2c00070**.

51 Z. Z. Lin, X. H. Li and H. B. Kraatz, impedimetric Immobilized DNA-Based Sensor for Simultaneous Detection of Pb^{2+}, Ag^{+}, and Hg^{2+}, *Anal. Chem.*, 2011, **83**, 6896–6901, DOI: **10.1021/ac2014096**.

52 Keysight 16452A Liquid Test Fixture, **https://www.keysight.com/zz/en/assets/9018-01431/user-manuals/9018-01431.pdf**.

53 R. M. Hill, Characterization of dielectric loss in solids and liquids, *Nature*, 1978, **275**, 96–99, DOI: **10.1038/275096a0**.

54 H. Hiura, T. W. Ebbesen and K. Tanigaki, Opening and purification of carbon nanotubes in high yields, *Adv. Mater.*, 1995, **7**, 275–276, DOI: **10.1002/adma.19950070304**.

55 C. Geyik, S. Evran, S. Timur and A. Telefoncu, The Covalent Bioconjugate of Multiwalled Carbon Nanotube and Amino-

Modified Linearized Plasmid DNA for Gene Delivery, *Biotechnol. Prog.*, 2014, **30**, 224–232, DOI: **10.1002/btpr.1836**.

56 D. H. Jung, B. H. Kim, Y. K. Ko, M. S. Jung, S. Jung, S. Y. Lee and H. T. Jung, Covalent attachment and hybridization of DNA oligonucleotides on patterned single-walled carbon nanotube films, *Langmuir*, 2004, **20**, 8886–8891, DOI: **10.1021/la0485778**.

57 Keysight E4990A Impedance Analyzer, **https://www.keysight.com/zz/en/product/E4990A/impedance-analyzer-20-hz-10-20-30-50-120-mhz.html**.

58 Keysight 16048G 1 m Port Extension Cable for Impedance Analyzer, **https://www.keysight.com/zz/en/product/16048G/1m-port-extension-cable-impedance-analyzer.html**.